Materials & Design 212 (2021) 110282

Contents lists available at ScienceDirect

Materials & Design

journal homepage: www.elsevier.com/locate/matdes

Understanding creep in TiAl alloys on the nanosecond scale by molecular dynamics simulations

Hariprasath Ganesan [a,*], Ingo Scheider [a], Christian. J. Cyron [a,b]

[a] Institute of Material Systems Modeling, Helmholtz-Zentrum Hereon, Geesthacht, Germany
[b] Institute for Continuum and Material Mechanics, Hamburg University of Technology, Hamburg, Germany

HIGHLIGHTS

- The applied stress and microstructure model address the caveats of atomistic creep.
- Physically affine atomistic models reduce creep rates by three orders of magnitude.
- Dislocation gliding (strain bursts) and colony boundary sliding dominate the creep.
- Interlamellar interfaces inhibit both the dislocation nucleation and its mobility.

GRAPHICAL ABSTRACT

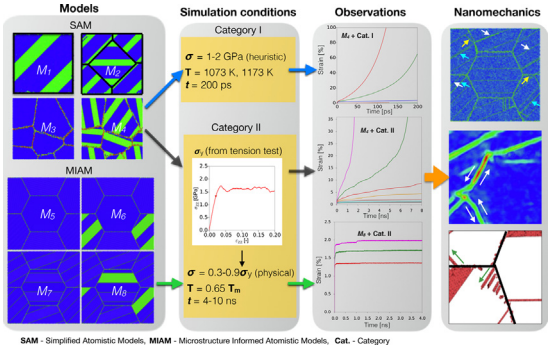

ARTICLE INFO

Article history:
Received 19 August 2021
Revised 17 November 2021
Accepted 23 November 2021
Available online 24 November 2021

Keywords:
Molecular dynamics
Creep
Atomistic modeling
TiAl alloys
Poly-colony
Nanocrystalline
Nanomechanics

ABSTRACT

Molecular dynamics (MD) simulations of creep generally face the problem that the creep most often evolves on time scales hard to capture with MD due to their typically short time step size. Consequently, MD studies of creep often use unrealistically high temperatures and stresses and simplified atomistic models to make creep-like processes happen on computationally accessible time scales. Apparently, this compromises the physical reliability of such studies. To alleviate this problem, we designed an MD model of titanium aluminide (TiAl) with a microstructure matching at least many of the key parameters of experimentally observed microstructures. We applied this MD model with stresses much lower than the ones used in most previous creep studies (well below yield stress) and in the temperature range $0.55T_M - 0.7T_M$, with melting temperature T_M. Compared to typical previous MD studies, this much more realistic setup produces creep rates more than three orders of magnitude smaller and thus much closer to reality. We identified the driving mechanisms of primary creep on the nanosecond scale that agree very well with recent experimental observations, thus contributing towards the overarching goal of bridging the gap between atomistic creep simulations and continuum-scale creep simulations for engineering applications.

1. Introduction

The aviation industry demands more fuel-efficient aero engines with significantly smaller CO_2 and NO_x footprints due to growing concerns about climate change. Such environment-friendly engines require lightweight materials with high strength and service

* Corresponding author.
E-mail address: hariprasath.ganesan@hereon.de (H. Ganesan).
URL: https://www.hereon.de (H. Ganesan).

https://doi.org/10.1016/j.matdes.2021.110282
0264-1275/

temperatures since an increase in the turbine inlet temperature by 10°C improves the engine efficiency by 1% [1]. In this area, gamma titanium aluminide γ(TiAl)-based alloys have attracted increasing attention. These ordered intermetallic compounds combine high specific strength and moduli with excellent corrosion resistance even at high service temperatures [2]. These properties make γ-(TiAl)-based alloys increasingly replace conventional single crystal superalloys for the rotating components in aero engines, for example, the turbine blades [3,4].

By suitable processing, γ(TiAl)-based alloys can be produced with four different microstructures, namely duplex, nearly gamma, nearly lamellar, and fully lamellar microstructure [3]. These four microstructures mechanical properties range from excellent high temperature creep resistance, fracture toughness, strength to tensile ductility. In particular, the fully lamellar microstructure excels for high-temperature applications [4]. This microstructure typically consists of two intermetallic phases for engineering applications: γ-TiAl (ordered face-centered tetragonal - $L1_0$) and α_2-TiAl (ordered hexagonal - DO_{19}). The constituent intermetallic phases form a platelet-like structure consisting of so-called lamella [1]. Several lamellae are stacked together in an identically oriented fashion to form so-called colonies. Accordingly, fully lamellar TiAl exhibits a complex microstructure with hierarchical interfaces across the length scales starting from colony interfaces (highest level) to single-lamellar interfaces (lowest level).

Creep refers to time-dependent inelastic (*permanent*) deformation under stresses below the yield stress. It typically accelerates with increasing temperature. Thus, in practice, creep resistance and structural stability of γ(TiAl)-based alloys are limiting the service temperature in aero engines [5]. Continuous efforts have been made to improve the creep resistance of two-phase γ(TiAl)-based alloys by tailoring the microstructure [6]. In parallel, continuum-mechanical modeling contributed to understanding their microstructure-property relationship [7] significantly. A recent study [8] pointed out the shortcomings of the existing creep models of fully lamellar TiAl alloys and concluded that for realistic creep simulations, not only bulk creep but also interfacial creep should be taken into account, e.g., by cohesive zone models [9–11].

While continuum mechanics has substantially contributed to our understanding of the creep of TiAl on the meso- and macroscale, it cannot unravel its atomistic and nanomechanical foundations. To this end, molecular dynamics (MD) simulations are required. While over the last years, a considerable number of MD studies of TiAl alloys have been published [12–22], only two recent studies specifically addressed creep [23,24], however, with several serious limitations like unrealistic TiAl atomistic models combined with heuristic stresses for creep simulation. This is particularly surprising, noting that over the last two decades MD simulations of creep in metallic materials have attracted rapidly increasing attention [25–39]. They helped understand the relation between creep deformation mechanisms and thermo-mechanical conditions on the nanoscale. Moreover, they yielded atomistically informed parameters for creep calculations on larger length scales. So far, MD simulations of creep in metallic materials typically suffer from several important limitations. First, to keep the computational cost feasible, very small systems are often studied, resulting in models with a nanocrystalline structure rather than a physically rigorous microcrystalline one (e.g., TiAl alloys). Second, current MD models of metal creep usually assume very high stresses and temperatures. This automatically induces a high strain rate. Consequently, most of these studies observed the three main creep stages (primary, secondary and tertiary creep) within time scales accessible by MD simulations, ranging from a few hundred picoseconds to a few nanoseconds. Note that the rapid deformation resulting from such high applied stresses, some times above σ_y, violates creep conditions per definition.

These limitations are important because the high volume fraction of grain boundaries in nanocrystalline materials considerably decreases the creep resistance compared to microcrystalline structures, as observed typically in TiAl [33]. Moreover, the combination of high stress and temperature typically assumed activates either the dislocation or diffusion-driven mechanisms, constrained by the nanocrystalline topology and Hall-Petch effects, again limiting the scope that can be addressed with MD simulations. This way, the currently made modeling assumptions severely limit the transferability of atomistic insights from MD creep simulations to real TiAl.

In summary, four critical issues have to be revisited on the way to more realistic MD creep models: the magnitude of the applied stress, the type of microstructure model, the temperature level, and the strain rate. In this work, we study the influence of the first three issues on the fourth issue with a focus on TiAl alloys. To this end, we study herein altogether eight different atomistic models of TiAl creep, which differ from each other by their degree of realism. They range from highly simplified models under unphysically high assumed stresses - in many respects similar to the models studied so far in the literature - up to MD models with a largely realistic microstructure combined with realistic loading and service temperature. That is, the applied stress lies in the range $\sigma = 0.3\sigma_y - 0.9\sigma_y$ (with yield stress σ_y) and the applied temperatures in the range $0.55T_M - 0.7T_M$ (with melting temperature T_M). We demonstrate that such conditions reduce the creep strain rate by around three orders of magnitude compared to previous similar MD studies of creep in metallic materials, bringing our models much closer to a realistic regime. Such realistic atomistic models and optimal thermo-mechanical conditions enhance the physical reliability of the observed nanomechanisms during MD creep simulations, which are in agreement with several experimental works [5,6,40-45]. Though the strain rates and time scale considered in our study are still much faster than under typical service conditions, these improvements enable us to gain new insights into the atomistic mechanisms of creep in γ(TiAl)-based alloys.

2. Materials and methods

2.1. Atomistic modeling of γ-TiAl alloy

At the atomic scale, materials can be modeled as many-body systems consisting of a finite number of particles that represent atoms. MD can accurately capture the thermal, mechanical, chemical, and thermodynamic behavior of such systems, however, within the adequacy of the interatomic potential. Herein, we used the MD code LAMMPS [46] (*Large-scale Atomic Molecular and Massively Parallel Simulator*). To describe the interactions between atoms, we used the so-called embedded atom method (EAM) [47] type potential for the TiAl system developed by Zope and Mishin in [48]. This EAM potential has already been successfully used in several MD studies, including ours of γ(TiAl)-based alloys [14,22,49]. It correctly predicts the lattice constants, cohesive energy, and elastic constants of α_2-Ti_3Al, even though this information was not explicitly part of the data used for fitting the parameters of the potential.

γ(TiAl)-based alloys for engineering applications usually consist of two intermetallic phases: γ-TiAl (ordered face-centered tetragonal - $L1_0$ structure) and α_2-Ti_3Al (ordered hexagonal - DO_{19} structure) [3]. In our TiAl models, we considered the lattice parameters a_0 = 3.998 Å and c/a_0 = 1.047 for the γ-TiAl phase [48] along with the crystallographic X-direction [1 $\bar{1}$ 0], Y-direction [1 1 $\bar{2}$], and Z-direction [1 1 1]. Similarly, we chose the

lattice parameters for the α_2-Ti_3Al phase as a_0 = 5.7884 Å and c/a_0 = 0.820 along with the crystallographic X-direction [1 $\bar{1}$ 0], Y-direction [1 1 0], and Z-direction [0 0 1].

These two phases are arranged in stacked lamellae [1]. Several lamellae with identical orientation form so-called colonies, as shown in the experimentally observed microstructure (Fig. 1). The thickness of individual lamellae ranges on the order of 10^1–10^3 nm and their aspect ratio can be as large as 10^3. The size of colonies is on the order of micrometers.

Herein we model colonies with either one intermetallic phase (γ-TiAl) or two such phases, namely γ-TiAl and α_2-Ti_3Al. Accordingly, we refer to such models using the qualifier 'single-phase' or 'two-phase'. In general, there are both γ/γ and γ/α_2 interlamellar interfaces [22]. The γ/α_2 interface is generally aligned with the close-packed plane and direction, i.e., $\{1\,1\,1\}_\gamma||(0\,0\,0\,1)_{\alpha_2}$ [1]. The γ/γ interfaces always share the same [1 1 1] direction, and in real materials, the phases are rotated by a multiple of 60° around this axis relative to each other. In the simulated model, we only consider one particular γ/γ interface with a rotation of 60°, the so-called pseudo-twin (γ/γ_{PT}) interface.

Unlike the previous studies of MD creep in TiAl [23,24], we considered physically rigorous atomistic models and thermo-mechanical conditions expected in component's service scenario. Therefore, in this study, we focus on understanding the implications of both the microstructure model and the applied stress on the observed strain rate and associated nanomechanics.

Typically, a fully lamellar TiAl microstructure can be characterized by the following key parameters: thickness of γ lamellae λ^γ, thickness of α_2 lamellae λ^{α_2}, α_2 volume fraction φ^{α_2}, separation distance of α_2 lamellae d^{α_2}, and characteristic colony size λ_C. Note that the experimentally reported lamellar thicknesses typically represent the average value of the thickness distribution [7,50].

Herein we consider eight different atomistic models $M_i, i = 1,\ldots,8$ divided into two categories. The models M_1 - M_4 in the first category are referred to as simplified atomistic models (SAMs), M_5 - M_8 in the second category are referred to as microstructure-informed atomistic models (MIAMs). The SAMs resemble the type of MD model that has been mostly used in the literature [23–39] to study creep at an acceptable computational cost. To this end, they [23,24] use a highly simplified microstructure whose characteristic lengths are typically below the ones observed in reality (see also Table 1 and Table 2). By contrast, the domain sizes of the MIAMs are much larger than the ones of the SAMs, allowing for much more realistic representations of the microstructure, where MIAM M_8 exhibits characteristic lengths that are largely realistic (with the main exception of the colony size λ_C, which is still much smaller than in reality). Details of the microstructure of the MIAMs and how it compares to experimental observations are presented in Table 1 and Table 2.

2.1.1. Simplified atomistic models – SAMs

The four SAMs studied herein are illustrated in Fig. 2. M_1 and M_2 exhibit a simplified regular microstructure, M_3 and M_4 a more realistic random microstructure. All SAMs except for M_3 consist of both γ and α_2 lamellae, i.e., two-phase, whereas M_3 serves for studying the (rather fictitious) case of an absence of the α_2 phase. In Fig. 2, the different phases, interfaces, and colony (grain) boundaries can be visually distinguished by their specific centrosymmetry parameter (CSP) values. The CSP measures the local lattice disorder around an atom. It is thus sensitive to phase type, defects, surfaces, and interfaces. For atoms embedded in a defect-free γ-TiAl lattice, the CSP is zero. By contrast, for one in a defect-free α_2-TiAl lattice, it is 7. Even higher CSP values are reached in the neighborhood of dislocation cores, interfaces, colony boundaries, and surfaces.

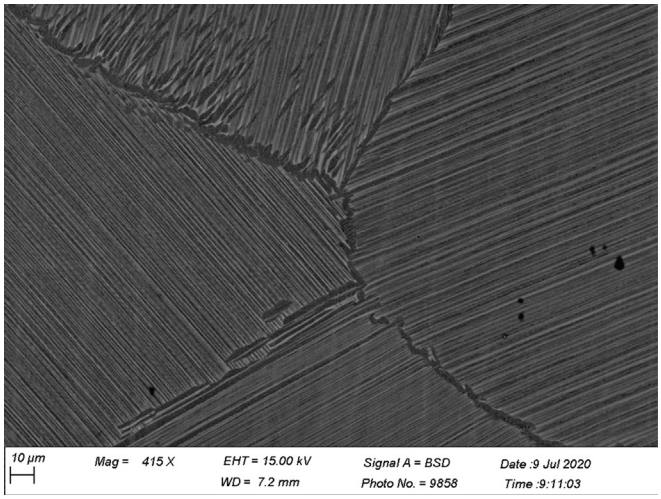

Fig. 1. A scanning electron microscope (SEM) image of the fully lamellar γ(TiAl)-based alloy with four neighboring colonies. A large number of γ and α_2 lamellae stacked in each colony with identical orientations.

Table 1
Microstructure parameters $\lambda^\gamma, \lambda^{\alpha_2}, \varphi^{\alpha_2}, d^{\alpha_2}$ of the 8 atomistic TiAl models studied herein compared to experimentally reported values [7,50].

Model	$\lambda^\gamma, \lambda^{\alpha_2}$ [nm]	φ^{α_2} [%]	d^{α_2} [nm]
M_1	8.66, 4.03	31.4	8.66
M_2	8.66, 4.03	29.9	8.66
M_3	9.18–17.96, –	–	–
M_4	4.49, 2.63	36.7	4.49
M_5	40, –	–	–
M_6	10.51–40, 10.21	12.0	10.51
M_7	10.53, –	–	–
M_8	10.53, 10.30	14.6	31.59
Ref. [7,50]	10 nm–1 µm	5–20%	10 nm–20 µm

Due to their simplicity, SAMs typically cannot resolve all relevant details of the microstructure. Rather they can only be used to study the role of specific microstructural features. The regular $\gamma + \alpha_2$ mono- and poly-colony SAM M_1 and M_2 are used to study the role of interfaces. By contrast, the poly-colony SAM M_3 and M_4 were designed to study in particular topological effects observed in the presence of a random colony structure (non-uniform shape/size). Moreover, as the only difference between M_3 and M_4 is the presence of the α_2 phase in the latter, it is instructive to compare these two models, since in real materials, the creep resistance of pure γ TiAl is not satisfactory.

The SAM M_1 has periodic domains of 22.6 nm × 20 nm × 20 nm with 5.3×10^5 atoms. Here, the lamellar interfaces form an angle of 45° w.r.t. to the Y direction. The SAM M_2 consists of five nano-sized colonies in a periodic domain of 11.6 nm × 40 nm × 40 nm with 1.07×10^6 atoms. The lamellar interfaces in this model's central cuboid colony form an angle of 0° w.r.t. to the Y direction, whereas this angle becomes 45° in the surrounding colonies. Asymmetries in the neighboring colonies were achieved by translation (colony ID: 2-5) and rotation (colony ID: 1). It is worth noting that in model M2, the borders of the structure are colony boundaries. The SAM M_3 and M_4 have a periodic domain of 30 nm edge length with 1.6×10^6 atoms. Their random colony structure was constructed by a Voronoi tesselation algorithm [51].

2.1.2. Microstructure-informed atomistic models – MIAMs

The four MIAMs M_5 - M_8 considered here have periodic domains of 20 nm × 80 nm × 80 nm with 7.5×10^6 atoms. Randomized

Table 2
Properties of real TiAl microstructures (left) and overview to which extent these are represented in the 8 atomistic TiAl models M_1 - M_8 studied herein.

Physical property	Model M_1	M_2	M_3	M_4	M_5	M_6	M_7	M_8
poly-colony	○	●	●	●	●	●	●	●
γ/α_2 interfaces	●	●	○	●	○	●	○	●
γ/γ_{PT} interfaces	○	○	○	○	○	○	●	●
uniform shape/size	○	○	○	○	●	●	●	●
$10\,nm \leqslant \lambda^{\gamma} \leqslant 1\,\mu m$	○	○	●	○	●	●	●	●
$10\,nm \leqslant \lambda^{\alpha_2} \leqslant 1\,\mu m$	○	○	○	○	○	●	○	●
$5\% \leqslant \varphi^{\alpha_2} \leqslant 20\%$	○	○	○	○	○	●	○	●
$10\,nm \leqslant d^{\alpha_2} \leqslant 20\,\mu m$	○	○	○	○	○	●	○	●
$10\,\mu m \leqslant \lambda_C \leqslant 1\,mm$	○	○	○	○	○	○	○	○

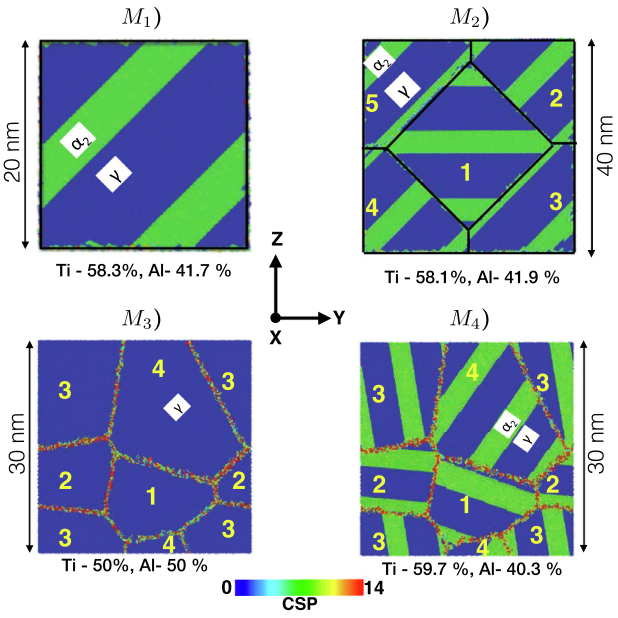

Fig. 2. Simplified atomistic models (SAMs) of γ-TiAl alloy: (M_1) $\gamma + \alpha_2$ mono-colony model with regular microstructure, (M_2) $\gamma + \alpha_2$ poly-colony model with regular microstructure, (M_3) γ poly-colony model with random microstructure, (M_4) $\gamma + \alpha_2$ poly-colony model with random microstructure. In poly-colony models the individual colonies are tagged by IDs.

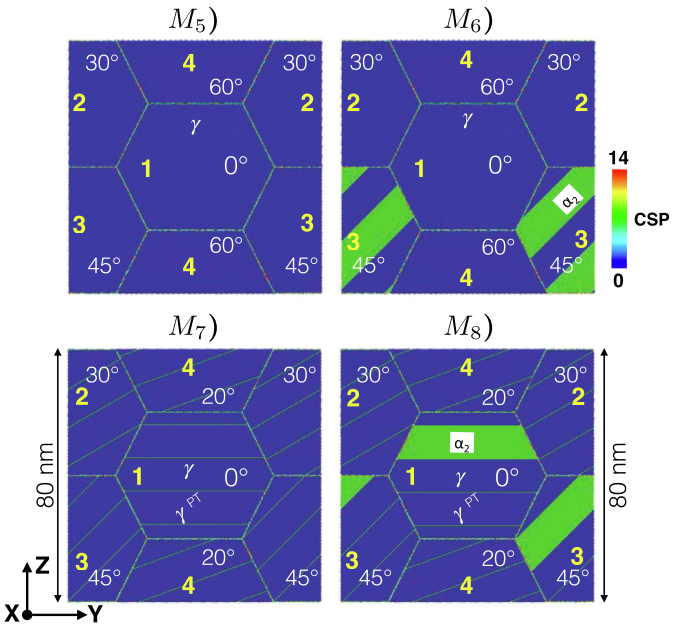

Fig. 3. Microstructure-informed atomistic models (MIAMs) of γ-TiAl alloy: (M_5) γ poly-colony model with a nearly gamma microstructure, (M_6) $\gamma + \alpha_2$ poly-colony model with a duplex microstructure, (M_7) $\gamma + \gamma_{PT}$ poly-colony model with a fully lamellar microstructure, (M_8) $\gamma + \gamma_{PT} + \alpha_2$ poly-colony model with a fully lamellar microstructure.

grain shapes in SAM (M_3, M_4) result in thermodynamic forces that contribute to grain shape changes. To eliminate such so-called topological driving forces [26] as far as possible, the MIAMs rely on regular colony shapes [27]. Hence, M_5 - M_8 use uniform hexagonal colonies (grains) with a grain size of 40 nm (Fig. 3). The crystallographic orientations of colony 1 in X-, Y-, and Z-direction were [1 $\bar{1}$ 0], [1 1 $\bar{2}$], and [1 1 1], respectively. The crystallographic orientations in the colonies 2–4 are rotated around the X-axis by 30°, 45°, and 60° or 20°. The only difference between M_5 and M_6 is the presence of the α_2 phase in the latter. As also for M_3 and M_4, this difference allows us to examine the effect of the presence of an α_2 phase and γ/α_2 interfaces. For MIAM M_7 and M_8, all colonies consist of lamellae. In M_7 only γ/γ_{PT} interfaces appear, resulting from the presence of a pseudo-twin (PT) γ_{PT} phase [22]. The difference between M_7 and M_8 is the additional presence of an α_2 phase in the latter. As apparent from Table 2, the microstructure of M_6 and M_8 are realistic with respect to the values of their characteristic parameters except for the colony size, which is unrealistically small (nanoscale rather than microscale) to keep the computational cost feasible. Compared to MIAM M_6, M_8 has a slightly higher φ^{α_2} and d^{α_2} (Table 1) and the α_2 phases are distributed over two colonies. MIAM M_5 and M_6 represent non-lamellar nearly gamma and duplex microstructure models, whereas MIAM M_7 and M_8 resemble the fully lamellar microstructures typically used in engineering. Yet, compared to the MD models used so far in the literature to study creep in TiAl [23,24], the MIAM can be considered a substantial step towards physical reality. In particular, M_6-M_8 allows us to study the contribution of lamellar γ/α_2 and γ/γ_{PT} interface creep in TiAl by MD simulations in a realistic setting.

2.2. MD simulation setup

2.2.1. Preprocessing

The preprocessing of our SAMs and MIAMs was performed in several steps. First, for each initial configuration, energy minimization was performed using FIRE and conjugate gradient algorithms in LAMMPS [46]. Then the minimized configuration was heated to 300 K with a subsequent constant temperature and pressure equilibration for 100 ps. Subsequently, the temperature in the models was increased at 2.57 K ps^{-1} up to the target temperature, where another equilibration was performed, first for 300 ps at constant pressure (to obtain the target volume) and then for another 300 ps at constant volume (to distribute the kinetic energy evenly within the model). The heating and equilibration simulations were realized using a Nosé-Hoover thermostat with a time step size of

1 fs and periodic boundary conditions. All the MD simulations herein were performed in a realistic temperature range $0.55T_M - 0.7T_M$, with melting temperature T_M.

2.2.2. Creep simulations

We applied isobaric isothermal (NσT) conditions using the Parrinello-Rahman technique [52] and periodic boundary conditions to study creep by two categories of simulations. The creep response will be discussed in terms of three stages: (1) primary creep - creep strain slowly increases, however, with a decreasing creep rate, (2) secondary creep - creep strain steadily increases at a constant creep rate, (3) tertiary creep - creep strain exponentially increases with accelerating creep rate.

Category I (unphysically high stress): in this category, we adopted the approach of many previous MD studies of creep (e.g., [23,24]) and assumed an unphysically high stress above yield stress to accelerate creep in our simulations and reduce thereby the computational cost. Our four SAMs were subjected to uniaxial tensile stresses of 1000 MPa, 1500 MPa, and 2000 MPa in Z-direction for 200 ps. In X- and Y-direction, we applied pressure of 0 bar. Time step size was 2 fs. As shown in Table 3, σ_y in our SAMs typically ranges between 1.28 GPa and 1.32 GPa so that the applied stresses in *Z*-direction of 1500 MPa, and 2000 MPa are unphysically high. In category I, we performed all simulations at the two temperatures $0.65T_M = 1073K$ and $0.71T_M = 1173K$ with the melting temperature of TiAl $T_M = 1650K$.

Category II (realistic stress): in this category, we considered the physically much more realistic stress range in *Z*-direction $0.3\sigma_y - 0.9\sigma_y$ with yield stress σ_y. To compute σ_y uniaxial tension tests were simulated at a temperature of $0.65T_M$ and a strain rate of $10^9/s$. A study of the role of the strain rate would be instructive but was beyond the scope of our study. In category II, we studied the SAM M_3 and M_4 with a pressure of 0 bar in X- and Y-direction and a time step size of 2 fs. The MIAMs M_5 - M_8 were simulated with the (even slightly more realistic atmospheric) pressure of 1 bar in X- and Y-direction and a time step size of 1 fs to resemble reality as accurately as possible with these most detailed MD models.

2.2.3. Postprocessing

Postprocessing and visualization of results were performed using in-house scripts together with the visualization tool OVITO [53]. The following quantities were evaluated:

Atomic displacements: $\mathbf{d} = \mathbf{r}_t - \mathbf{r}_0$, that is, the difference between the current position $\mathbf{r}_t$ of an atom and its initial position $\mathbf{r}_0$.

Shear strain: the shear strain denotes the local (scalar) shear invariant (after [54]) of the Green-Lagrangian strain tensor $\mathbf{E} = 1/2(\mathbf{F}^T\mathbf{F} - \mathbf{I})$ computed using the atomic strain modifier [53]. Here, $\mathbf{F}$ and $\mathbf{I}$ indicate deformation gradient and identity tensor. The scalar shear strain field helps to visualize and characterize defects in atomic systems under deformation.

Dislocation density: The evolution of the dislocation density was analyzed using the dislocation-identification algorithm DXB [55], calculating the dislocation density $\rho_{Dis} = l_{Dis}/\Omega_{box}$ as a ratio between the total dislocation length l_{Dis} and the volume of the simulation domain Ω_{box}.

Common neighbor analysis: The local structural environment of an atom, e.g., crystalline phase or defect, was characterized using the common neighbor analysis (CNA) algorithm.

Table 3
σ_y identified from the uniaxial tension tests (Fig. 7) for 6 models M_3 - M_8 at a temperature of $0.65T_M = 1073K$.

Model	σ_y [GPa]
M_3	1.280
M_4	1.327
M_5	1.250
M_6	1.125
M_7	1.450
M_8	1.250

3. Results

3.1. Category I (unphysically high stress)

Fig. 4 shows the temporal evolution of creep strains over 200 ps for the four different SAMs in our creep simulations of category I.

3.1.1. SAM M_1 and M_2: mono-colony and poly-colony

For the lowest stress of 1000 MPa, both the mono- and the poly-colony SAM with regular microstructure, M_1 and M_2, revealed only a primary creep stage. For the medium stress of 1500 MPa, additionally a secondary creep stage, and for the highest stress of 2000 MPa, even a tertiary creep stage are observed. There are two main differences between the regular mono- and poly-colony SAM. First, insensitivity to temperature is observed for the former, suggesting mainly stress-driven deformation mechanisms such as mechanical twinning, stress-induced α_2 transformation, and dislocation motion. These mechanisms observed in MD simulations, e.g., mechanical twinning and stress-induced phase transformation, especially under high stresses, confirm previous experimental claims [1,42]. By contrast, the temperature dependence of creep is observed in the latter for the medium and highest stress. This suggests that the activation of temperature-driven deformation mechanisms there requires considerable mechanical driving forces. The second important difference between the mono-colony and poly-colony SAM is the much faster creep in the latter. As the main difference between the mono-colony SAM and the poly-colony SAM is the existence of colony (grain) boundaries, the faster creep in the poly-colony SAM can most likely be attributed to the presence of these boundaries, highlighting their key role in TiAl alloys creep.

Note that the orientation of the lamellar interfaces is most likely not the reason for the increased creep rate in the case of the poly-colony SAM M_2. For there, the colonies 2–5 exhibit the same orientation of the lamellar interface w.r.t the loading direction as the mono-colony model (so-called soft mode/ 45° to loading direction), and the central colony 1 has a lamellar orientation perpendicular to the loading direction (so-called hard mode [1]), which should rather decrease than increase the creep rate. Fig. 5 illustrates the evolution of the atomic displacement in the Z-direction d_z (relative to the initial configuration) and the microstructure evolution. Indeed colony 1 (hard-mode) exhibits the lowest creep displacements, as expected from its loading perpendicular to its lamellar interfaces.

It is instructive to examine the mechanisms responsible for the large creep deformation in the poly-colony SAM M_2, particularly in colonies 3 and 5. To this end, we computed the atomic shear strains at 200 ps. As shown in Fig. 6, peak regions of atomic shear strains correspond to regions of twinning and considerable colony boundary sliding, identifying, in particular, the latter of these two mechanisms as a main nanomechanical driver of the deformation. In Fig. 6(a), green arrows indicate the direction of the twinned and parent region of the intermetallic γ phase. Finally, note that the

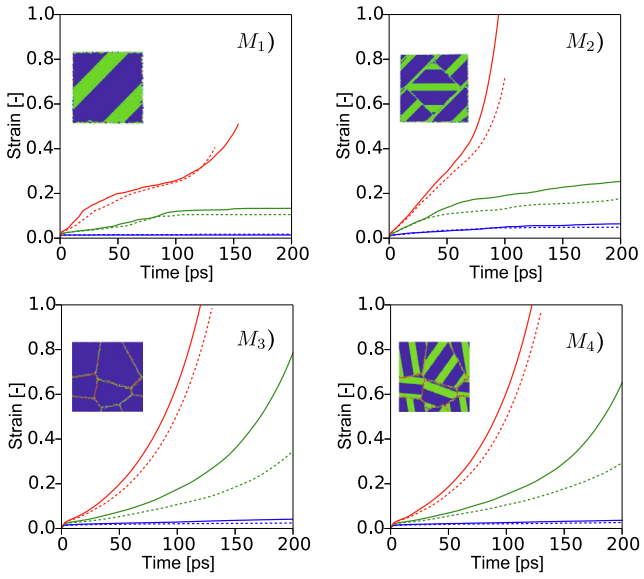

Fig. 4. Creep simulations of category I: creep strain evolution under different uniaxial tensile stresses and temperatures for the four SAMs: (M_1) $\gamma + \alpha_2$ mono-colony model with regular microstructure, (M_2) $\gamma + \alpha_2$ poly-colony model with regular microstructure, (M_3) γ poly-colony model with random grain structure, (M_4) $\gamma + \alpha_2$ poly-colony model with random grain structure.

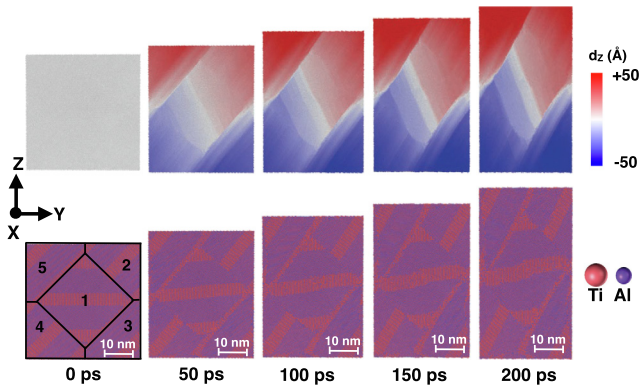

Fig. 5. Displacement in Z-direction d_z (top) and the evolution of microstructure (bottom) in regular $\gamma + \alpha_2$ poly-colony SAM M_2 under uniaxial tensile stress of 1500 MPa at 1173 K.

intermetallic α_2 phase in grain 1 shows a rift-like structure to accommodate twin transfer from the neighboring γ lamellae [1].

3.1.2. SAM M_3 and M_4 : γ and $\gamma + \alpha_2$

Both random poly-colony SAM M_3 and M_4 in Fig. 4 show a similar magnitude and temperature dependence of the creep strain for each of the three applied stresses. As already for the regular mono-colony and poly-colony SAM M_1 and M_2, and likely for the same reasons, temperature effects are observed only for the medium and highest stress. We observe a primary creep stage at all stresses but only at the medium and highest stress, also a secondary and tertiary creep stage. In nanocrystalline materials, the bulk dislocation activation volume is typically larger than the grain size, hampering the associated contributions to inelastic deformation. Consequently, the high colony (grain) boundary volume fraction dominates inelastic deformation even at high temperatures. Like many previous studies [23,24] with MD models similar to our SAMs, our random poly-colony models are also dominated by colony boundary effects.

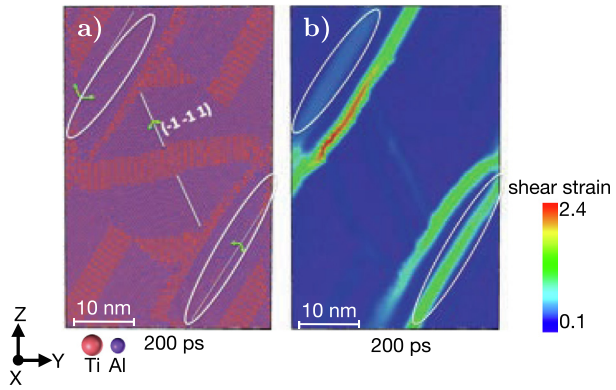

Fig. 6. Mechanical twinning in regular $\gamma + \alpha_2$ poly-colony SAM M_2 under uniaxial tensile stress of 1500 MPa at 1173 K: (a) in the microstructure regions of twinning and considerable colony boundary sliding correspond to (b) peak regions of atomic shear strains.

3.1.3. Discussion

Among the four different SAMs M_1 – M_4 studied, in category I, the regular $\gamma + \alpha_2$ mono-colony lamellar SAM M_1 shows the highest creep resistance. This can be explained by the absence of topological creep contributions from colony boundaries. It is noteworthy that also in the SAM with γ/α_2 interfaces, we observe substantial creep deformations due to dislocation-dominated mechanisms, although in a recent study [22] γ/α_2 interlamellar interfaces were found to form barriers to incoming dislocations from the γ phase under loading normal to the interface. While our computational study of different SAMs provided some insights into the nanomechanics of creep in TiAl, the SAMs suffer from severe limitations similar to previous MD studies [23,24], as pointed out above. In most key aspects, their microstructure is substantially different from real TiAl microstructures (Table 1, 2). The short simulation periods are a consequence of unphysically high applied stresses. However, these also lead to unphysical behavior such as dislocation-mediated inelastic deformation and damage within a few hundred ps. Indeed, stresses partially even above σ_y put into question to which extent the observed deformation can be classified as a classical creep. Generally, the unphysical magnitude of the applied stresses severely compromises the transferability of atomistically computed parameters, for example, to meso- or macro-scale continuum models.

3.2. Category II (realistic stress)

In category II, we considered the poly-colony SAM M_3 and M_4 and MIAMs M_5 - M_8. The most important difference between both categories is the much larger domain size of the latter, allowing for resemblance to real microstructures in all key aspects except for the colony size. The yield stresses σ_y of the six models M_3 - M_8 were determined in simulated uniaxial tensile tests. Fig. 7 shows the stress σ_{zz} vs. strain ε_{zz} in these tests in Z-direction. The yield stress σ_y was identified in these tests by determining the stress σ_{zz} at the onset of substantial dislocation activation [31] causing irreversible plastic deformation. The identified values of σ_y are

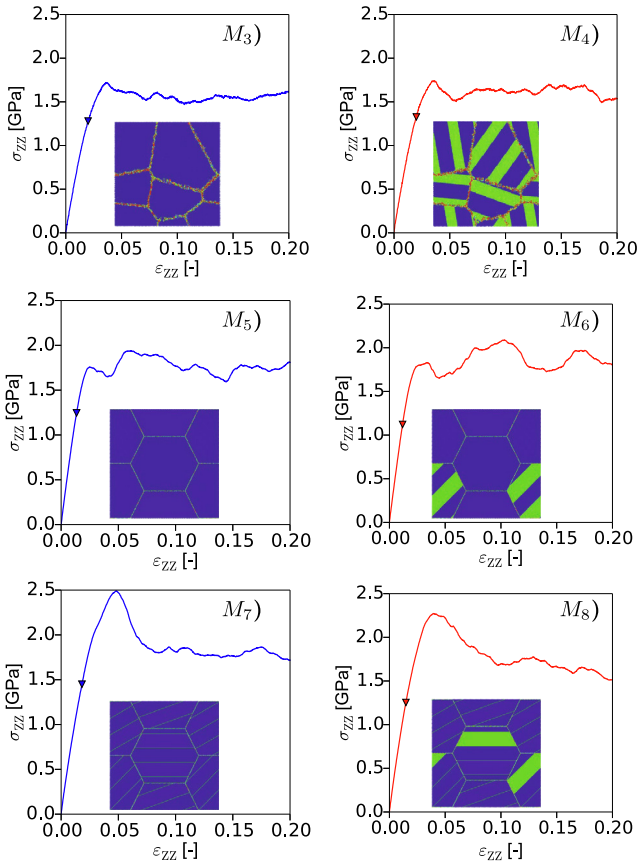

Fig. 7. Uniaxial tensions tests to determine yield stress σ_y at temperature $0.65T_M$ for the 6 models M_3 - M_8. Observed σ_y are marked by triangles.

listed in Table 3. Note that the computed σ_y of the different MIAMs show the following hierarchy $\sigma_y(M_6 - Duplex) < \sigma_y(M_5 - NG) \leqslant \sigma_y(M_7, M_8 - FL)$, where NG and FL refer to Nearly Gamma and Fully Lamellar microstructure, respectively. This hierarchy is in perfect agreement with the experiment [42], thus, physically reliable MD models.

The creep simulations in category II focus on the primary and secondary creep stage because these are most relevant during the lifetime of high-temperature engineering materials like TiAl. Tertiary creep mainly determines how such materials fail at the end of their lifetime. Nevertheless, it is worth noting that the simulations are spanning several nanoseconds, while only 200 ps were simulated in the previous category I.

3.2.1. SAM M_3 and M_4 : γ and $\gamma + \alpha_2$

Observations: In the low-stress range $0.3\sigma_y$ to $0.5\sigma_y$, both random poly-colony SAM experience only very small creep strains with only a primary creep regime (Fig. 8 a, c). For $0.6\sigma_y$, additionally, secondary creep is observed, and for $0.7\sigma_y$ and beyond show even tertiary creep. The $\gamma + \alpha_2$ SAM M_4 shows a much higher creep resistance than the γ SAM M_3, at least for $\sigma \geqslant 0.6\sigma_y$.

Discussion: Generally, the high grain boundary volume fraction in nanocrystalline materials restricts bulk dislocation activity and favors grain-boundary-dominated mechanisms [56]. For nanocrystalline Cu, Wang et al. [28] observed a transition from grain boundary diffusion as dominant creep mechanism to grain boundary sliding with increasing stress and eventually dislocation-driven creep. The SAM M_3 and M_4 are both nanocrystalline. This suggests that the acceleration of creep with increasing stress observed in Fig. 8 may be understood from a similar transition to more effective deformation mechanisms. To examine this aspect, we computed the evolution of the dislocation density ρ_{Dis} during creep (Fig. 8 b, d). For $0.9\sigma_y$ and $0.8\sigma_y$, ρ_{Dis} increases exponentially for both SAM M_3 and M_4, suggesting dislocation-driven creep indeed at high stresses. For low stresses $\leqslant 0.7\sigma_y$, both M_3 and M_4 exhibit a nearly constant ρ_{Dis} over time, suggesting that in this regime creep is not dislocation-dominated, but grain boundary sliding. The stress-dependent role of dislocation-driven creep is also illustrated in Fig. 9, showing the CNA computed microstructure evolution of SAM M_3 in the stress range $0.7\sigma_y$ to $0.9\sigma_y$. At high stress ($0.9\ \sigma_y$), we observe numerous planar faults traced by dislocations originated from colony boundaries traversing the colony within 1000 ps. This phenomenon significantly declines with the level of applied stress (even for a much longer time), in agreement with the idea of a transition to non-dislocation-dominated deformation mechanisms in the low-stress regime.

In SAM M_4, the dislocation density at high stresses increases more slowly than in SAM M_3 (Fig. 8 b, d). Attributing this to the only difference between both models, the presence of an α_2 phase in M_4 underlines the role of γ/α_2 interfaces in hampering the motion of dislocations. The hindrance stems from the α_2 phase crystallographic configurations with restricted and incompatible slip systems for incoming dislocations from the γ phase [22]. Indeed, a similar phenomenon has been reported for nano-twinned metals [34].

To keep the computational cost low, many MD studies of creep have focused so far on nanocrystalline materials such as SAM M_3 and M_4 discussed in this section (TiAl [23,24] and others [25–39]). While such studies can certainly provide important insights, they also reveal that grain-boundary-based mechanisms govern the creep deformation at low stresses. This implies, however, that the high volume fraction of grain boundaries in nanocrystalline materials makes their creep resistance remarkably low, as pointed out already by [33]. As a consequence, the results of MD simulations of nanocrystalline systems can only to a very limited extent be translated to the technologically much more relevant microcrystalline systems. A step towards such systems will be done in the next section.

3.2.2. MIAM M_5 and M_6 : γ and $\gamma + \alpha_2$

Observations: Fig. 10 shows the creep strain evolution for the two MIAM M_5 and M_6. The difference between both is the presence of an additional α_2 phase in M_6. Pure γ microstructures, as in M_5, are typically not used for high-temperature applications in practice due to their poor creep resistance. However, here they can help to identify the contributions of γ/α_2 interfaces to creep in the $\gamma + \alpha_2$ MIAM.

In the γ poly-colony MIAM M_5 we observe high creep strain from an avalanche of strain bursts (jump events) in the beginning, followed by slowly increasing strain for the applied stress $0.9\sigma_y$. Such high creep deformation is attributed to colonies with pure γ phase and without any interlamellar interfaces that could hinder dislocation mobility. The magnitude of strain bursts reduces with decreasing applied stress. Generally, the pure γ microstructure M_5 appears more susceptible to creep. The addition of the α_2 phase and the resulting γ/α_2 interfaces appear to enhance the creep resistance relatively in M_6. As shown in the insets in Fig. 10, the dislocation density does not change significantly during the simulations. This suggests that the dislocation creep observed in the SAM models M_3 and M_4 is a result of the much larger topological driving forces that arise due to randomized grain shapes.

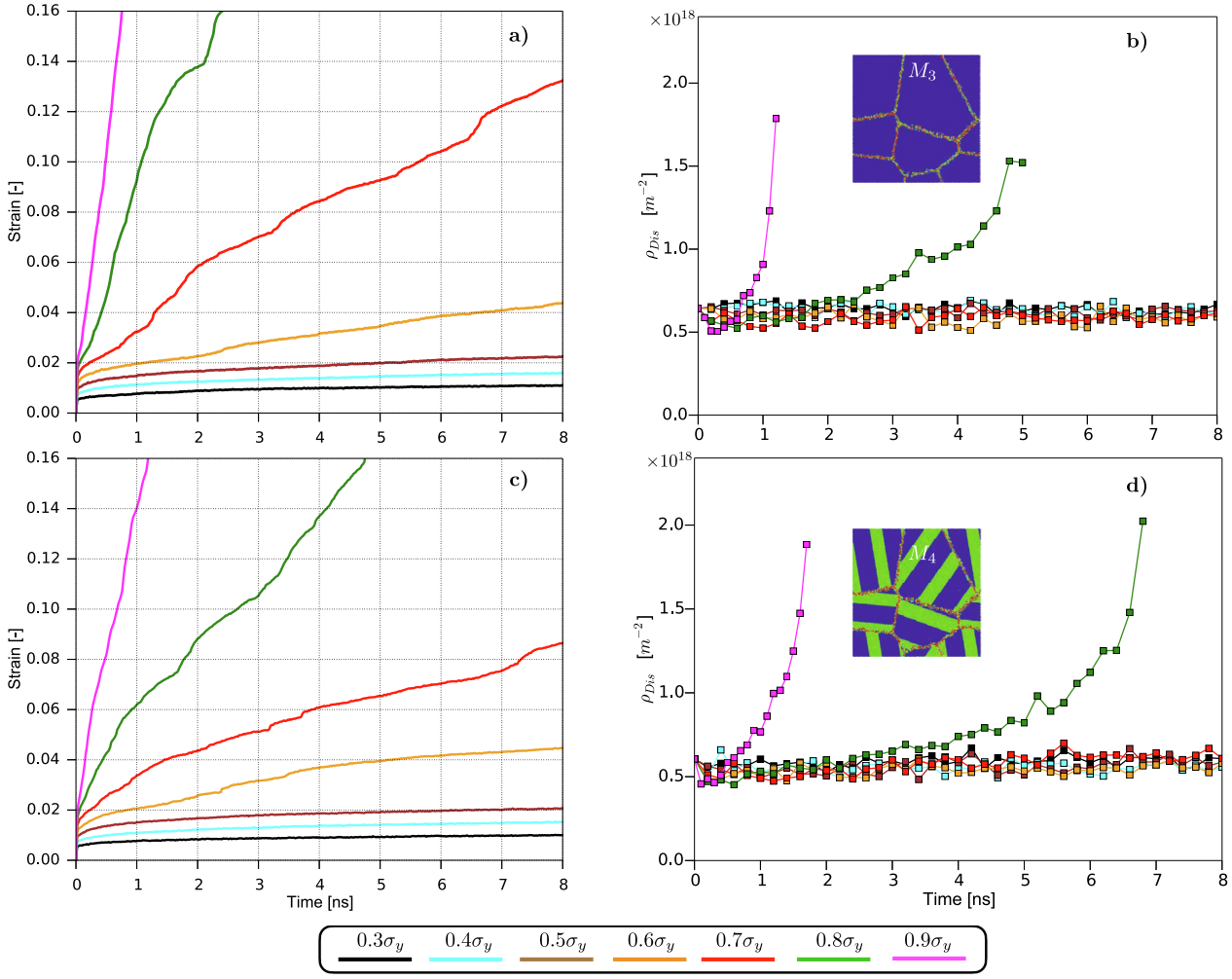

Fig. 8. Creep strain (a, c) and dislocation density evolution (b, d) of the two random poly-colony SAM M_3 and M_4 for the applied stresses (σ = 0.3σ_y - 0.9σ_y) at a temperature of $0.65T_M = 1073K$, where the σ_y of the corresponding model is taken from Table 3.

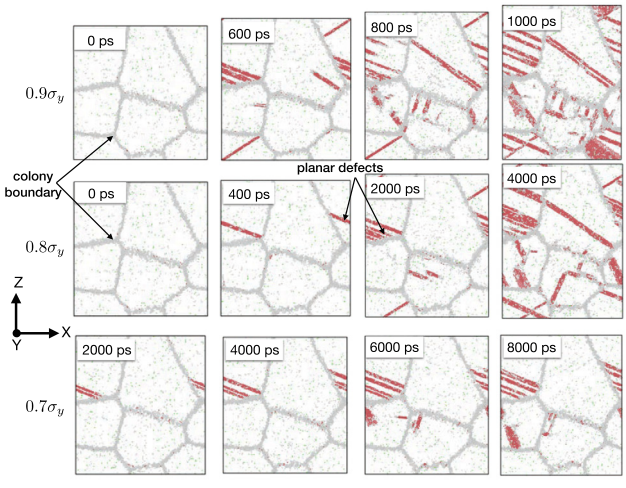

Fig. 9. CNA illustrates the evolution of colony boundaries (grey) and planar defects (red) in SAM M_3 during creep at stresses 0.9σ_y (top), 0.8σ_y (middle), and 0.7σ_y (bottom). Note the different time periods in the three rows.

Fig. 11 shows the creep strain evolution of the $\gamma + \alpha_2$ poly-colony MIAM M_6 over an extended period of 10 ns[1]. After 4 ns, no further strain bursts are observed. The initial period of strain bursts can thus be interpreted as a primary creep stage, stress and temperature not being high enough to stimulate visible secondary creep within the period simulated.

Fig. 12 shows the creep strain evolution in the $\gamma + \alpha_2$ MIAM M_6 for different temperatures at a constant stress 0.8σ_y, where σ_y is the yield stress at temperature $0.65T_M = 1073K$. Generally, the magnitude of strain bursts increases with temperature. The particularly high strain jump at 973 K forms an outlier that could not be explained within this study. In a previous study [22] we found that the yield stress σ_y decreases with increasing temperature. Combining those results and the observations here, the higher magnitude

[1] This MPI parallelized simulation took around 12 days of computation time on our HPC cluster (2.1 GHz Intel® Xeon Platinum Skylake processor equipped with Intel® Omni-Path high-speed network switch for communication) using 216 cores. Thus, giving an estimate of the computational demand of realizing such large and long MD simulation.

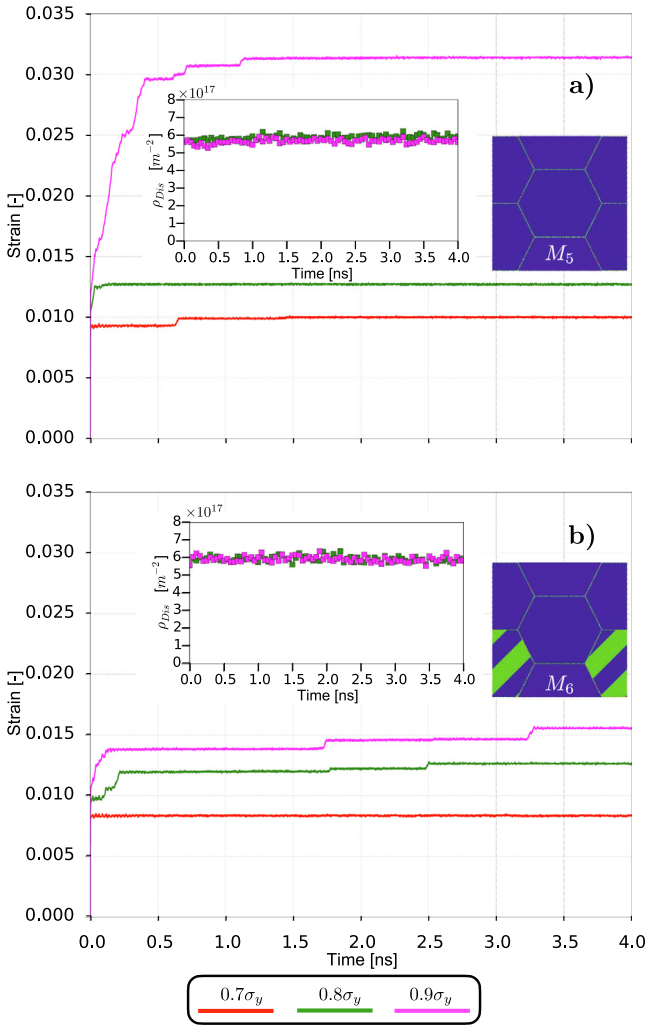

Fig. 10. Creep strain evolution for MIAM M_5 (top) and M_6 (bottom) at temperature $0.65T_M = 1073K$. The inset for M_5 and M_6 shows the evolution of the dislocation density.

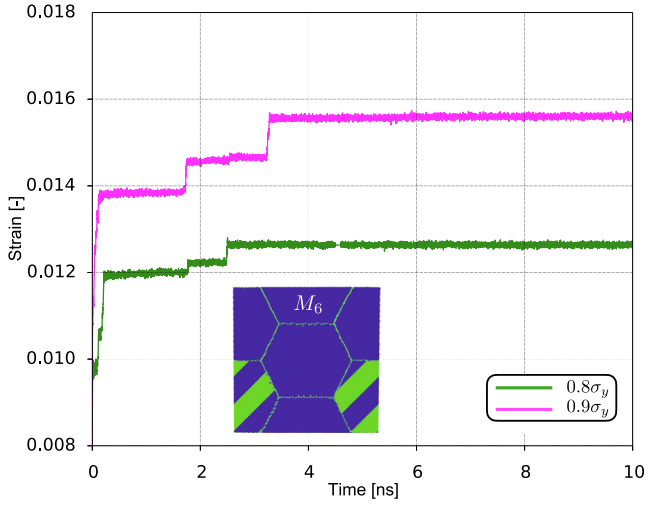

Fig. 11. Creep in $\gamma + \alpha_2$ MIAM M_6 over an extended period at two different stress levels and temperature $0.65T_M = 1073K$.

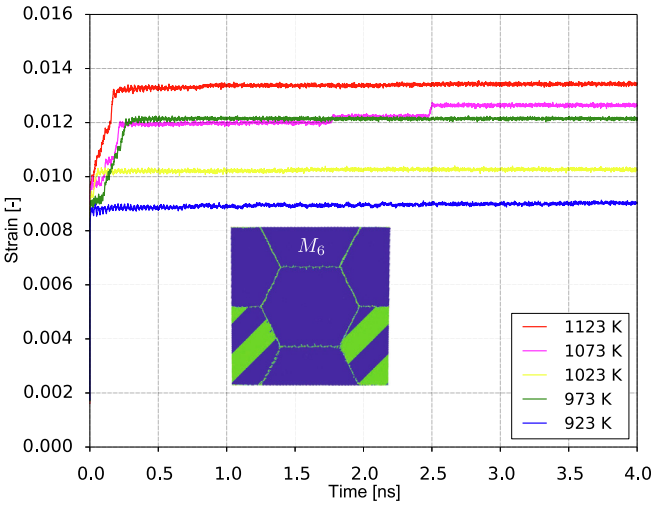

Fig. 12. Creep deformation in $\gamma + \alpha_2$ MIAM M_6 at stress $0.8\sigma_y(0.65T_M)$ for different temperatures.

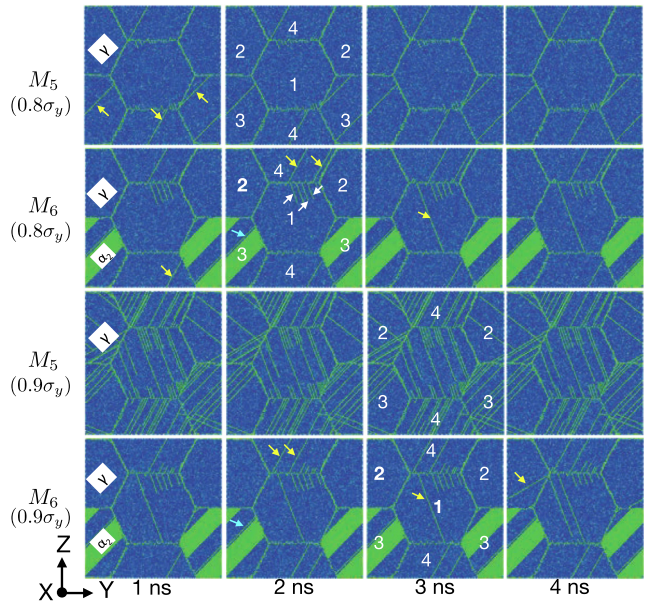

Fig. 13. Microstructure evolution of the MIAM M_5 and M_6 at stresses $0.8\sigma_y$ and $0.9\sigma_y$ and temperature $0.65T_M = 1073K$. Colony IDs are printed in white as a guidance for the discussion. Apparently, a sequence of dislocation glide events (marked by arrows) is responsible for the strain bursts (jumps) driving creep in MIAM M_6.

of strain jumps with temperature may be explained by the fact that with increasing temperature the applied stress corresponds to an increasing fraction of yield stress (at that temperature).

To understand the role of the strain bursts driving primary creep, we compared the microstructural evolution at two different stresses between M_5 and M_6 (Fig. 13). At stress $0.8\sigma_y$, M_5 shows dislocation nucleation from the colony boundary triple junctions 2/4/1 and 3/4/1 and the colony boundary 1/3 (yellow arrows). The dislocations traverse along the glide plane until encountering a colony boundary. There, their further mobility is hindered due to an insufficient driving force to cross the colony border and change their glide plane thereby. Consequently, the central colony 1 with hard orientations shows no considerable dislocation glide activities. By contrast, at the higher stress $0.9\sigma_y$, the driving forces for dislocation motion are high enough to cause a host of concerted

dislocation glide activities also across colony boundaries resulting in an avalanche of strain bursts. For MIAM M_6 at the stress $0.8\sigma_y$, a dislocation nucleated from colony boundary 3/4 glides (yellow arrow at time 1 ns). Also, a twinning dislocation (blue arrow at time 2 ns) from colony boundary 1/3 traverses colony 3, forming a twin boundary (1 1 1)[1 1 $\bar{2}$]. Note that, in M_6 even at the stress $0.9\sigma_y$ dislocation gliding appears considerably impeded (Fig. 13).

Discussion: Combining Fig. 10 and Fig. 13, we conclude that the atomistic origin of the strain bursts observed in MIAM M_5 and M_6 is the nucleation and gliding of dislocations. Note that both increases with stress, as does also the strain bursts driven creep. We underline that this interpretation is not in contradiction to the nearly constant dislocation density ρ_{Dis} shown in the insets in Fig. 10. MIAM M_5 and M_6 exhibit already considerable initial dislocation densities due to misfit dislocations at colony boundaries. However, most of these dislocations remain sessile due to unfavorable slip systems and thus do not contribute to creeping. Note that creep is driven by the few dislocations gliding and the relatively small number of new dislocations nucleating. Nevertheless, the number of the latter is small because dislocation emission from colony boundaries requires a relatively high localized activation stress [29]. Thus, in our simulations, the number of nucleating dislocations remained much smaller than the number of initially existing dislocations so that no visible increase of the total dislocation density was observed over time.

Recently, [57] reported strain bursts for nano-creep experiments in semi-crystalline polymers and assumed the origin of these bursts in dislocation mobility. Our MD simulations support this interpretation. Thus, they not only unravel for the first time strain bursts as a nano-creep mechanism in TiAl but also contribute to our understanding of creep beyond the specific case of TiAl.

Noting that dislocation nucleation at colony boundaries plays an important role in the strain bursts driving creep, it is instructive to study its origin. Fig. 14 reveals the nucleation of two dislocations from the 1/2 colony boundary (white arrows in Fig. 14d). Interestingly, this nucleation directly follows substantial colony boundary sliding indicated by a high atomic shear strain (yellow arrows in Fig. 14b, c), suggesting that colony boundary sliding acts as an assisting precursor mechanism of dislocation nucleation. These nanomechanical insights from MD creep simulations validate the predictability of the unified creep formula based on dislocation glide and colony boundary sliding by Zhang and Deevi [42], who proposed following the careful analysis of several experimental works of various TiAl alloys in a broad temperature range 600–900 °C. It is worth noting that no previous MD works reported such colony boundary sliding precursor mechanism in TiAl alloys.

Comparing M_5 and M_6, the latter exhibits considerably higher creep resistance at the macroscale associated with considerably impeded nucleation and gliding of dislocations at the atomic scale (Fig. 13). Noting the difference between M_5 and M_6 is only the presence of α_2 lamellae in the latter, this simulation result is in excellent agreement with the experimentally well-known positive effect of the α_2 phase on the creep resistance of TiAl alloys [1].

3.2.3. MIAM M_7 and M_8 : γ+ γ_{PT} and $\gamma + \gamma_{PT} + \alpha_2$

Observations: MIAM M_7 and M_8 contain both γ and γ_{PT} phases and thus γ/γ_{PT} lamellar interfaces. Additionally, M_8 includes an α_2 phase and γ/α_2 interfaces. Fig. 15 shows the creep strain evolution in M_7 and M_8 with their fully lamellar microstructure. At the beginning, both M_7 and M_8 exhibit instantaneous strains proportional to the applied stresses followed by a very slow increase in strain indicating a primary creep regime (transient creep) for the simulated time. In line with our above discussion, M_8 with its additional α_2 phase and γ/α_2 interfaces appears more resistant to creep than

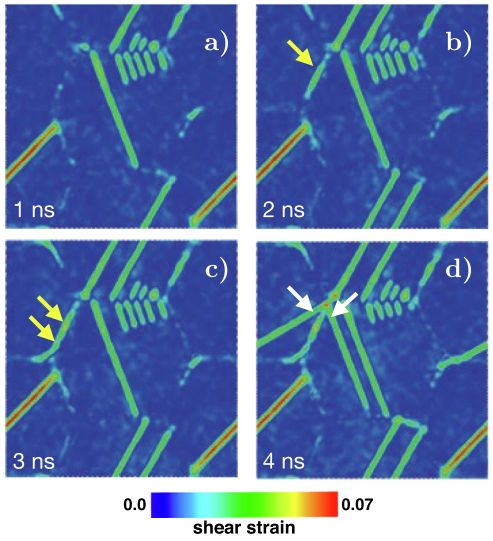

Fig. 14. Atomic shear strain in the $\gamma + \alpha_2$ MIAM M_6 at stress $0.9\sigma_y$ and temperature 1073 K. High strain indicates slipped (green) and twinned (red) regions. Colony boundary sliding (yellow arrows) occurs as a precursor mechanism of dislocation slip (white arrows).

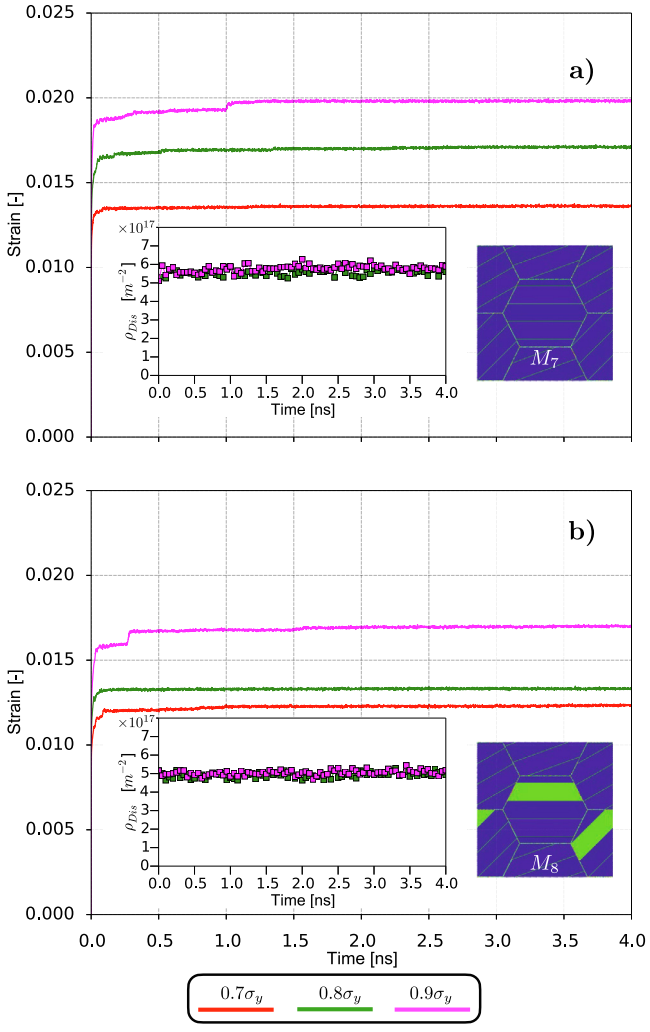

Fig. 15. Creep strain evolution in M_7 (top) and M_8 (bottom) at temperature $0.65T_M = 1073K$ with the inset showing the corresponding dislocation density evolution.

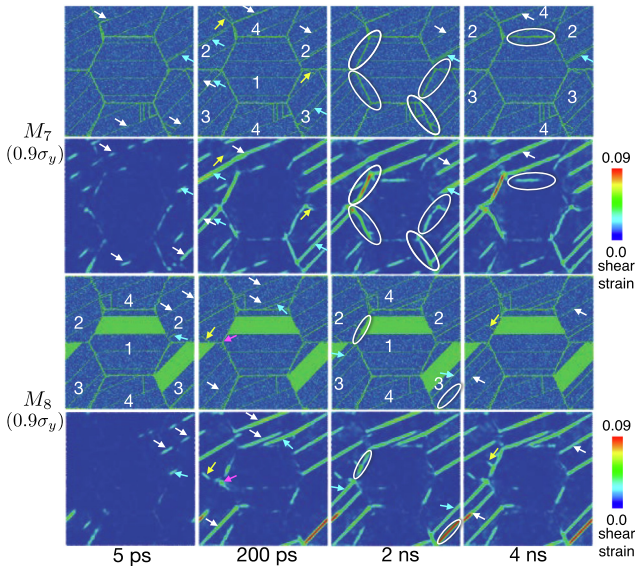

Fig. 16. Microstructure and atomic shear strain in M_7 (1st and 2nd row) and M_8 (3rd and 4th row) at stress $0.9\sigma_y$ and temperature $0.65T_M = 1073K$. Arrows indicate dislocation gliding and elliptical markers highlight colony boundary sliding.

M_7. The insets of Fig. 15 reveal negligible changes in the total dislocation density, which is also in line with the above discussion of M_5 and M_6.

However, unlike M_5 and M_6, M_7 and M_8 exhibit no significant strain jump events except for the highest applied stress $0.9\sigma_y$. To examine the nanomechanical origin of creep, Fig. 16 compares the microstructure and atomic shear strain evolution for M_7 and M_8 at the stress $0.9\sigma_y$ at the points in time 5 ps, 200 ps, 2 ns, and 4 ns.

In M_7, dislocations nucleate predominantly from the junction of colony boundary and lamellar interface. Strain imbalance across the lamellar interface also contributes to a few dislocation nucleation events, as reported in experiments [58]. At the beginning (after 5 ps), interfacial gliding, i.e., dislocation gliding along the γ/γ_{PT} lamellar interfaces, marks the onset of creep. Interestingly, interfacial gliding dislocations as the resulting creep mechanism from our MD simulations agree with the experimental work on fully lamellar TiAl [6]. As time progresses, there exist three dislocation propagation mechanisms: (1) interfacial gliding (white arrows), (2) gliding on planes parallel to the lamellar interface (blue arrows), and (3) gliding on planes oblique to the lamellar interface (yellow arrows). Generally, the dislocation gliding is impeded by γ/γ_{PT} lamellar interfaces (*hampering gliding on oblique planes*), colony boundaries (*hampering interfacial gliding and gliding on parallel planes*), and dislocation-dislocation interactions. After 2 ns, the colony boundaries 1 and 3 undergo substantial sliding resulting in shear strain. Thus, colony boundaries act as both source and sink for dislocations.

Compared to M_7, one observes in M_8 (Fig. 16) the same three dislocation propagation mechanisms. For dislocation nucleation, M_8 shows not only colony boundary junctions but also homogeneous colony boundaries between two γ regions (blue arrows after 5 ps) and heterogeneous colony boundaries between γ and α_2 regions (yellow arrow after 200 ps) as nucleation sites. In M_8, the additional α_2 phase greatly reduces colony boundary sliding (elliptical markers), dislocation nucleation and propagation. For example, in colony 3, the α_2 phase suppresses interfacial glide along γ/α_2 interfaces. Consequently, in colony 3, dislocation gliding is limited to γ/γ_{PT} lamellar interfaces and planes parallel to γ/α_2 interfaces in γ regions.

Under the given thermo-mechanical conditions, in our MD simulations, dislocation gliding (arrows) and colony boundary sliding (elliptical markers) appears to dominate the primary creep (Fig. 16). Thus, any hindrance to these two mechanisms can be expected to reduce creep. Compared to the γ phase, both the γ_{PT} and α_2 regions appear to contribute negligibly to the atomic mechanisms of creep. In M_7 and M_8, the interfaces govern the creep deformation, whereas in M_5 and M_6, also some bulk contribution exists. This observation agrees with the experimentally reported creep on nearly gamma TiAl microstructure (like our M_5), which suggests that primary creep is caused by dislocation gliding both on lamellar interfaces and γ lamellae (bulk) [40].

Discussion: For the applied thermo-mechanical conditions, M_7 and M_8 show a slow creep strain evolution. Our MD MIAMs captured several experimentally reported nanomechanical events (e.g., dislocation gliding [40,41], colony boundary sliding [42], interfacial glide [6], and dislocation emission from interfaces [5,43,44]) during creep deformation. In Fig. 17, we comprehensively depicted the observed dislocation-based nanomechanical events from our MD creep simulations. Dislocation-based nanomechanical events categorized into nucleation, propagation, and hindrance govern the observed creep. Unlike in M_5 and M_6, there were no significant strain jump events in MIAM M_7 and M_8 (except at $0.9\sigma_y$) due to the fully lamellar microstructure, which seems to lead to the absence of sequential gliding activities spanning several colonies and additionally a severely reduced dislocation gliding distance. In M_5 and M_6, the dislocation gliding predominantly occurs in pure γ colonies, where the gliding distance is proportional to the colony size λ_C. By contrast, in M_7 and M_8, this distance reduces to the lamellar spacing λ^{γ}. This nanomechanical insight from MD simulation holds in perfect agreement with the experimental works [41,45,59], which claim a decrease in primary creep strain with decreasing lamellar spacing in fully lamellar microstructure (like our M_7 and M_8).

Trapped dislocations at lamellar interfaces and colony boundaries hinder subsequent interfacial gliding and other oncoming dislocations [1,41]. Dislocation locking occurs when two cross-gliding dislocations encounter, providing additional resistance to further dislocations mobility. These MD results for MIAM M_7 and M_8 confirm the following experimental observations about creep mechanisms in fully lamellar TiAl [41,45]: lamellar interfaces may (1) inhibit dislocation gliding such that a fine lamellar spacing reduces the gliding distance; (2) trap dislocation segments, restricting dislocation motion.

Qualitatively, our MD simulations of dislocation propagation agree with the experiments reported in [6,40,41], which show dislocation motion at and along the γ/γ and γ/α_2 interfaces. Hence, interface sliding contributes to the strain, especially in the primary creep regime. Interestingly, the microstructure of the TiAl in [6] had the lamellar thicknesses of $\lambda^{\gamma} = 100 \ldots 300$nm ($10^1$ higher than in our simulations) and $\lambda^{\alpha_2} = 10 \ldots 50$nm (same order), which make the microstructure largely comparable to the one in our MD simulations. Note, however, that our MIAM M_7 and M_8 exhibit smooth colony boundaries, whereas the ones in [6] were serrated, which likely reduced colony boundary sliding due to interlocking. Interestingly, however, also our MD simulations showed only slight colony boundary sliding, which thus appears to be of no significant importance (at least on the length and time scale considered herein).

In our MD simulations, the central colony (ID 1) significantly assisted to dislocation gliding and creep in M_5 and M_6 but not in M_7 and M_8 (Fig. 16). The reason is the presence of the γ/γ_{PT} and γ/α_2 interfaces in the latter. These are subject to nearly normal

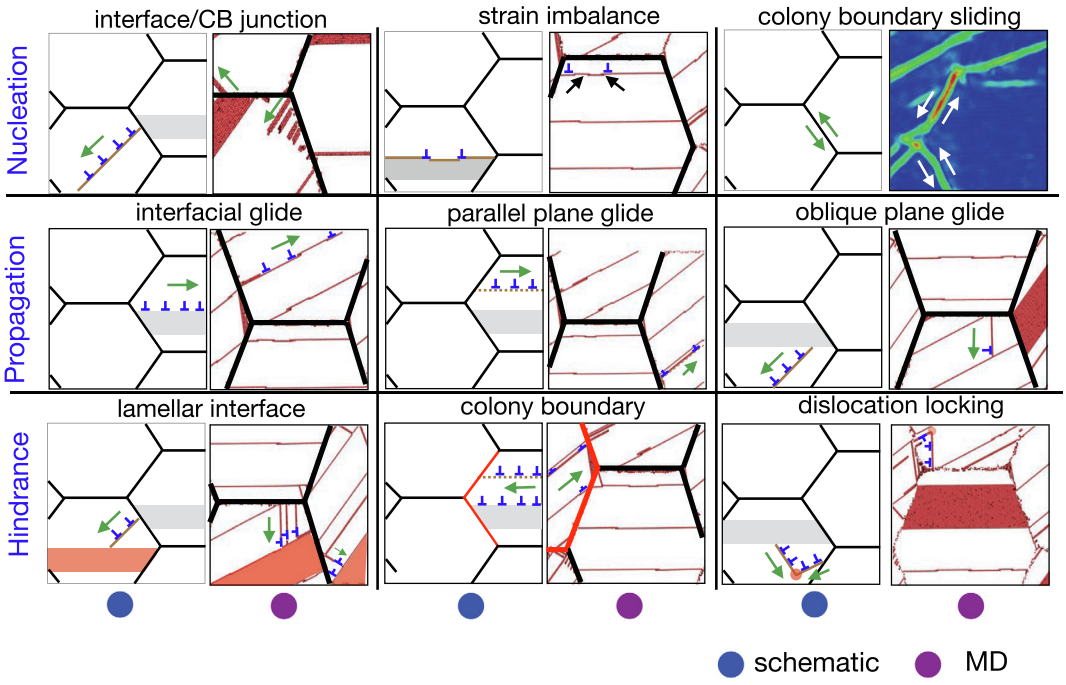

Fig. 17. Schematics and MD simulated snapshots illustrating different dislocation-based nanomechanics (nucleation (top), propagation (middle), hindrance (bottom)) contributing to creep in MIAM M_7 and M_8.

loading in colony 1, resulting in minimal deformation (hard mode) [22]. Chen et al. [60] reported restricted dislocation mobility due to fine lamellar spacing in softly oriented grains and retarded shear in hard oriented grains. Also, well-interlocked lamellae along colony boundaries resist intergranular cracking, hampering dislocation nucleation. In our models, the absence of preexisting interfacial dislocations and the high applied stresses (although below σ_y) enabled dislocation nucleation from colony boundaries and strain imbalance [58] near the lamellar interfaces resulting in gliding on interlamellar interfaces and on its parallel planes (Fig. 17). Thus, our simulations show dislocation nucleation from colony boundary triple junctions and heterogeneous regions.

Fig. 18 compares the creep rate (computed as mean creep rate between the two points in time 1ns and 4ns) vs. applied stress for the SAM M_3 and M_4 with the three of the MIAMs M_6-M_8, whose microstructures are in many respects close to the ones used in reality for engineering applications. The creep rate of the $\gamma + \alpha_2$ SAM M_4 is always slightly lower than the one of the pure γ SAM M_3, which can be understood from the creep-impeding presence of γ/α_2 interfaces as discussed already above. Interestingly, [32] reported a similar observation for nanotwinned models with decreased twin boundary spacing. Compared to SAM M_3 and M_4, the creep rate in MIAM M_6 is reduced by two orders of magnitude. We suggest that there are two main reasons for this. On the one hand, the MIAM like M_6 exhibit regular colony shapes. In contrast, the random colony shape in the SAM M_3 and M_4 can be expected to give rise to topological driving forces resulting in larger inelastic deformation. On the other hand, the colony (grain) size in the MIAM M_6 is considerably larger than in the SAM M_3 and M_4, which can be expected to reduce grain boundary effects and thus also associated creep substantially. In fact, several studies on nanocrystalline models reported reducing creep rates for increasing grain size [29,33,35]. In the future, more comprehensive parameter studies separately varying the different microstructural parameters $(\lambda^{\gamma}, \lambda^{\alpha_2}, d^{\alpha_2})$ could help to deepen our understanding of this phenomenon. The fully lamellar TiAl models M_7 and M_8 exhibit creep

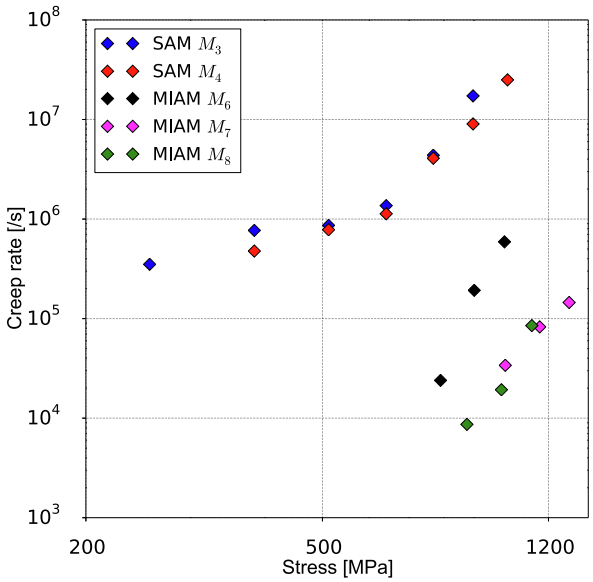

Fig. 18. Influence of microstructure on creep strain rate at given stress level at temperature $0.65T_M$.

rates that are even around one order of magnitude smaller than the ones of M_6, underlining the creep inhibiting effect of the lamellar structure discussed above and well-known from experiments [1,6,45,61–63]. Among M_7 and M_8, M_8 seems slightly more resistant against creep, underlining the creep-inhibiting role of the α_2 phase. The reduced creep rate of the fully lamellar MIAM M_7 and M_8 compared to the duplex model M_6 results not only from reduced dislocation propagation but also from reduced dislocation nucleation by inhibited colony boundary sliding. Altogether, the combination of physically rigorous MIAMs and realistic applied stress in our MD creep simulations aid in predicting both the

nanomechanics and the strain rate hierarchy for different microstructures considered herein, qualitatively.

4. Summary & conclusions

Over the last years an increasing number of MD studies of creep has been proposed for TiAl [23,24] and other metallic materials [26–39]. These studies typically focused on nanocrystalline and nanotwinned materials. The reported creep mechanisms include grain boundary diffusion (Coble and Nabarro-Herring creep), grain boundary sliding, and grain-boundary-assisted dislocation nucleation and motion. They can thus be broadly classified into diffusion-driven and dislocations-driven creep. Typically these studies considered very small simulation domains together with high stress (for dislocation-driven creep) and high temperature (for diffusion-driven creep) to observe creep-like phenomena within a time scale accessible to MD. However, as discussed herein on the basis of simplified atomistic models (SAMs) that resemble those previously used in MD creep studies, this leads to highly unphysical phenomena such as creep rates so high that tertiary creep occurs within a few hundred picoseconds. Such rapid deformation is rather the time scale of fracture than the one of creep. Hence, insights gained from such MD simulations may be misleading, in general not only quantitatively but even qualitatively. For such a short time scale may not allow studying deformation mechanisms whose activation takes considerable time but which may yet dominate in the long run. In particular, it is often not possible to observe the thermal activation of deformation mechanisms on very short time scales [64]. To this end, SAMs exposed the limitations of the previous MD creep studies.

This paper's major objective is to point out how these caveats of current MD creep models can be overcome, at least to some extent. As a first step, we tested the effect of decreasing stress and temperature to a more realistic regime than most previous studies [23,24]. That is, we decreased stress clearly below yield stress σ_y to the regime $0.3\sigma_y$ - $0.9\sigma_y$ and temperature clearly below melting temperature to the regime $0.55T_M$ - $0.7T_M$. As we demonstrated, this decreases the creep rate (for the same microstructure) by around two orders of magnitude, thus, improving the physical reliability of our MD models. However, decreasing stress and temperature alone is insufficient because also the nanocrystalline structure used in most previous simulations substantially differs from the microstructure used in typical TiAl alloys for engineering applications. This is important because length scale also plays a crucial role in creep via the activation volume [28,64]. To address this aspect, we designed the microstructure-informed atomistic models (MIAMs) with a microstructure whose characteristic geometric parameters largely matched the ones experimentally observed (with the exception of the colony size, which still had to be chosen smaller than in typical engineering alloys to keep the domain size and thus computational cost acceptable). This decreased the creep rate by another two to three orders of magnitude. Effectively, this allowed us to study creep in TiAl - to our best knowledge for the first time - in a largely realistic microstructural setting and on the nanosecond scale. Due to the high computational cost of our simulations, only the primary creep regime could be studied. However, for this regime, we were able to identify as the main driving mechanism of creep on the atomic scale the nucleation of dislocations from colony boundaries and their gliding. Apparently, this mechanism is assisted by colony boundary sliding as a precursor mechanism and leads to a sequence of characteristic strain bursts that macroscopically results in primary creep. Interestingly, this observation is in excellent agreement with recent experimental observations reported by [57] for nano-creep experiments in semi-crystalline polymers.

Our MD simulations also confirmed the experimentally already known creep-reducing role of a fully lamellar microstructure [41,45]. The simulations revealed that such microstructures reduce the creep rate by around one order of magnitude. In particular, they demonstrated that this effect could be attributed to the inhibiting effect of the interlamellar interfaces on the nucleation and mobility of dislocations, which corroborates our understanding of the atomic foundations of the creep resistance of TiAl.

Altogether, our results demonstrate that for MD studies of creep, it is essential to set both temperature and stress to realistic values and use a microstructure that resembles the real one close enough to capture at least the essential phenomena on the atomic scale properly. Unlike the previous studies of MD creep in TiAl [23,24], our study showed a longer primary creep stage of realistic MIAM models besides capturing different underlying nanomechanical events driving creep. Furthermore, these observed nanomechanical events from MD creep simulations reaffirm the findings of several experimental works [5,6,40-45]. This way, our computational study could unravel the driving mechanism of - at least primary - creep on time and length scales not yet addressed so far by atomistic simulations in TiAl alloys. Such nanomechanical insights are an important step towards atomistically informed creep laws for mesoscale continuum models that are computationally efficient enough to capture the much longer time and length scales most relevant for engineering applications. We recommend incorporating our insights gained while investigating atomistic creep of other technological materials using MD simulations. Yet, we note that this paper is but a first step in this direction. A further extension of the time and length scale of our MD model will be required to bridge the gap to the mesoscale and continuum.

CRediT authorship contribution statement

Hariprasath Ganesan: Conceptualization, Methodology, Software, Writing – original draft. **Ingo Scheider:** Funding acquisition, Project Supervision, and Writing. **Christian. J. Cyron:** Project Supervision, Interpretation of results, Writing.

Data Availability

The raw/processed data required to reproduce these findings cannot be shared at this time as the data also forms part of an ongoing study.

Declaration of Competing Interest

The authors declare that they have no known competing financial interests or personal relationships that could have appeared to influence the work reported in this paper.

Acknowledgments

The authors gratefully acknowledge the funding of this project within the IDEA framework from Helmholtz-Zentrum Hereon (formerly Helmholtz-Zentrum Geesthacht), Germany.

Hariprasath Ganesan thanks Jonathan Paul for providing the SEM image used in this work and Jan Eike Schnabel for some fruitful discussions in the scope of this project.

References

[1] Fritz Appel, Jonathan David Heaton Paul, Michael Oehring, Gamma titanium aluminide alloys: science and technology, John Wiley & Sons, 2011.
[2] D.M. Dimiduk, Gamma titanium aluminide alloys – an assessment within the competition of aerospace structural materials, Mater. Sci. Eng. A 263 (2) (1999) 281–288.

[3] Helmut Clemens, Svea Mayer, Design, Processing, Microstructure, Properties, and Applications of Advances Intermetallic TiAl Alloys, Adv. Eng. Mater. 15 (4) (2013) 191–215.
[4] B.P. Bewlay, S. Nag, A. Suzuki, M.J. Weimer, TiAl alloys in commercial aircraft engines, Mater. High Temp. 33 (4–5) (2016) 549–559.
[5] Fritz Appel, Mechanistic understanding of creep in gamma-base titanium aluminide alloys, Intermetallics 9 (10–11) (2001) 907–914.
[6] L.M. Hsiung, T.G. Nieh, Creep deformation of fully lamellar TiAl controlled by the viscous glide of interfacial dislocations, Intermetallics 7 (7) (1999) 821–827.
[7] F. Appel, H. Clemens, F.D. Fischer, Modeling concepts for intermetallic titanium aluminides, Prog. Mater Sci. 81 (2016) 55–124.
[8] Jan Schnabel, Ingo Scheider, Crystal Plasticity Modeling of Creep in Alloys with Lamellar Microstructures at the Example of Fully Lamellar TiAl, Front. Mater. (2020).
[9] I. Scheider, Numerical Simulation of Material Separation Using Cohesive Zone Models, vol. 1, Springer, Singapore, 2018, pp. 1–42.
[10] Do Van Truong, Takayuki Kitamura, Cohesive zone model applied to creep crack initiation at an interface edge between submicron thick films, Int. J. Damage Mech. 19 (3) (2010) 301–319.
[11] Joachim Nordmann, Konstantin Naumenko, Holm Altenbach, A damage mechanics based cohesive zone model with damage gradient extension for creep-fatigue-interaction, Key Engineering Materials, vol. 794, Trans Tech Publ, 2019, pp. 253–259.
[12] Pengtao Li, Y.Q. Yang, Vladimir Koval, Jianxin Chen, Xian Luo, Wen Zhang, Bowen Wang, Haixue Yan, Temperature-dependent deformation processes in two-phase TiAl+ Ti3Al nano-polycrystalline alloys, Mater. Des. 199 (2021) 109422.
[13] Fu. Rong, Zhiyuan Rui, Yun Dong, Dechun Luo, Changfeng Yan, Effects of γ/γlamellar interfaces on interlamellar crack propagation behaviors of TiAl alloys, Comput. Mater. Sci. 194 (2021) 110428.
[14] Yang Chen, Yuede Cao, Zhixiang Qi, Guang Chen, Increasing high-temperature fatigue resistance of polysynthetic twinned TiAl single crystal by plastic strain delocalization, J. Mater. Sci. Technol. 93 (2021) 53–59.
[15] Ashish Chauniyal, Gerhard Dehm, Rebecca Janisch, On the role of pre-existing defects in influencing hardness in nanoscale indentations–Insights from atomistic simulations, J. Mech. Phys. Solids (2021) 104511.
[16] Yue Gao, Tinghong Gao, Lianxin Li, Quan Xie, Qian Chen, Zean Tian, Yongchao Liang, Bei Wang, Evolution of dislocation and twin structures in Ti3Al during solidification, Vacuum 194 (2021) 110525.
[17] Peng-tao Li, Yan-Qing Yang, Zhenhai Xia, Xian Luo, Na. Jin, Yong Gao, Gang Liu, Molecular dynamic simulation of nanocrystal formation and tensile deformation of TiAl alloy, RSC Adv. 7 (76) (2017) 48315–48323.
[18] Cao Hui, Rui Zhiyuan, Chen Wenke, Feng Ruicheng, Yan Changfeng, Deformation mechanisms in nanotwinned γ-TiAl by molecular dynamics simulation, Mol. Simul. 44 (18) (2018) 1489–1500.
[19] Wen Li, Yajun Yin, Qian Xu, Jianxin Zhou, Hai Nan, Xiaoyuan Ji, Xu Shen, Xin Feng, Wen Yu, Zhixin Tu, et al., Tensile behavior of γ/α2 interface system in lamellar TiAl alloy via molecular dynamics, Comput. Mater. Sci. 159 (2019) 397–402.
[20] Wen Li, Yu. Wen, Xu. Qian, Jianxin Zhou, Hai Nan, Yajun Yin, Xin Feng, Xu Shen, Effects of γ/γinterfaces in TiAl lamellae subjected to uniaxial tensile loading, Comput. Mater. Sci. 172 (2020) 109361.
[21] Wen Li, Wen Yu, Qian Xu, Jianxin Zhou, Hai Nan, Yajun Yin, Xu Shen, Understanding the atomistic deformation mechanisms of polycrystalline γ-TiAl under nanoindentation: Effect of lamellar structure, J. Alloys Compd. (2020) 154443.
[22] Hariprasath Ganesan, Ingo Scheider, Christian J Cyron, Quantifying the High-Temperature Separation Behavior of Lamellar Interfaces in γ-Titanium Aluminide Under Tensile Loading by Molecular Dynamics, Front. Mater. (2020).
[23] Fei Zhao, Jie Zhang, Chenwei He, Yong Zhang, Xiaolei Gao, Lu. Xie, Molecular Dynamics Simulation on Creep Behavior of Nanocrystalline TiAl Alloy, Nanomaterials 10 (9) (2020) 1693.
[24] Yongpan Zeng, Xiaoyan Li, Atomistic simulations of high-temperature creep in nanotwinned TiAl alloys, Extreme Mech. Lett. 44 (2021) 101253.
[25] P. Keblinski, D. Wolf, H. Gleiter, Molecular-dynamics simulation of grain-boundary diffusion creep, Interface Sci. 6 (3) (1998) 205–212.
[26] V. Yamakov, D. Wolf, S.R. Phillpot, H. Gleiter, Grain-boundary diffusion creep in nanocrystalline palladium by molecular-dynamics simulation, Acta Mater. 50 (1) (2002) 61–73.
[27] Paul C Millett, Tapan Desai, Vesselin Yamakov, Dieter Wolf, Atomistic simulations of diffusional creep in a nanocrystalline body-centered cubic material, Acta Mater. 56 (14) (2008) 3688–3698.
[28] Yun-Jiang Wang, Akio Ishii, Shigenobu Ogata, Transition of creep mechanism in nanocrystalline metals, Phys. Rev. B 84 (22) (2011) 224102.
[29] Yun-Jiang Wang, Akio Ishii, Shigenobu Ogata, Grain size dependence of creep in nanocrystalline copper by molecular dynamics, Mater. Trans. 53 (1) (2012) 156–160.
[30] Yun-Jiang Wang, Akio Ishii, Shigenobu Ogata, Entropic effect on creep in nanocrystalline metals, Acta Mater. 61 (10) (2013) 3866–3871.
[31] M.A. Bhatia, SN Mathaudhu, KN Solanki, Atomic-scale investigation of creep behavior in nanocrystalline Mg and Mg–Y alloys, Acta Materialia 99 (2015) 382–391, https://doi.org/10.1016/j.actamat.2015.07.068.
[32] Shuyin Jiao, Yashashree Kulkarni, Molecular dynamics study of creep mechanisms in nanotwinned metals, Comput. Mater. Sci. 110 (2015) 254–260.
[33] K.A. Darling, M. Rajagopalan, M. Komarasamy, M.A. Bhatia, B.C. Hornbuckle, R. S. Mishra, K.N. Solanki, Extreme creep resistance in a microstructurally stable nanocrystalline alloy, Nature 537 (7620) (2016) 378–381.
[34] Xu-Sheng Yang, Yun-Jiang Wang, Hui-Ru Zhai, Guo-Yong Wang, Yan-Jing Su, L. H. Dai, Shigenobu Ogata, Tong-Yi Zhang, Time-, stress-, and temperature-dependent deformation in nanostructured copper: Creep tests and simulations, J. Mech. Phys. Solids 94 (2016) 191–206.
[35] Kai Nie, Wu. Wen-Ping, Xian-Long Zhang, Shu-Mei Yang, Molecular dynamics study on the grain size, temperature, and stress dependence of creep behavior in nanocrystalline nickel, J. Mater. Sci. 52 (4) (2017) 2180–2191.
[36] Md Meraj, Snehanshu Pal, An Anomaly in Creep Property Dependence on Grain Size for Ultrafine Grain Nanocrystalline Nickel at Higher Creep Temperature, Materials Science Forum, vol. 978, Trans Tech Publ, 2020, pp. 477–486.
[37] Huan Yao, Tianzhou Ye, Yu. Wenshan, Pengfei Wang, Wu. Junmei, Wu. Yingwei, Ping Chen, Atomic-scale investigation of creep behavior and deformation mechanism in nanocrystalline FeCrAl alloys, Mater. Des. 206 (2021) 109766.
[38] Xiao-Ye Zhou, Ji-Hua Zhu, Wu. Hong-Hui, Xu-Sheng Yang, Shuize Wang, Xinping Mao, Unveiling the role of hydrogen on the creep behaviors of nanograined α-Fe via molecular dynamics simulations, Int. J. Hydrogen Energy 46 (14) (2021) 9613–9629.
[39] Md Habibur Rahman, Emdadul Haque Chowdhury, Sungwook Hong, Nature of creep deformation in nanocrystalline cupronickel alloy: A Molecular Dynamics study, Res. Mater. 10 (2021) 100191.
[40] J. Beddoes, D.Y. Seo, W.R. Chen, L. Zhao, Relationship between tensile and primary creep properties of near γ-TiAl intermetallics, Intermetallics 9 (10–11) (2001) 915–922.
[41] A. Chatterjee, H. Mecking, E. Arzt, H. Clemens, Creep behavior of γ-TiAl sheet material with differently spaced fully lamellar microstructures, Mater. Sci. Eng. A 329 (2002) 840–846.
[42] W.J. Zhang, S.C. Deevi, The controlling factors in primary creep of TiAl-base alloys, Intermetallics 11 (2) (2003) 177–185.
[43] L.M. Hsiung, T.G. Nieh, B.W. Choi, J. Wadsworth, Interfacial dislocations and deformation twinning in fully lamellar TiAl, Mater. Sci. Eng. A 329 (2002) 637–643.
[44] F. Appel, U. Christoph, M. Oehring, Creep deformation in two-phase titanium aluminide alloys, Mater. Sci. Eng. A 329 (2002) 780–787.
[45] C.E. Wen, K. Yasue, J.G. Lin, Y.G. Zhang, C.Q. Chen, The effect of lamellar spacing on the creep behavior of a fully lamellar TiAl alloy, Intermetallics 8 (5–6) (2000) 525–529.
[46] Aidan P. Thompson, H. Metin Aktulga, Richard Berger, Dan S. Bolintineanu, W. Michael Brown, Paul S. Crozier, Pieter J. in't Veld, Axel Kohlmeyer, Stan G. Moore, Trung Dac Nguyen, et al., LAMMPS-A flexible simulation tool for particle-based materials modeling at the atomic, meso, and continuum scales, Comput. Phys. Commun. (2021) 108171.
[47] Murray S Daw, Michael I Baskes, Embedded-atom method: Derivation and application to impurities, surfaces, and other defects in metals, Phys. Rev. B 29 (12) (1984) 6443.
[48] Rajendra R Zope, Yu Mishin, Interatomic potentials for atomistic simulations of the Ti-Al system, Phys. Rev. B 68 (2) (2003) 024102.
[49] S.P. Kiselev, E.V. Zhirov, Molecular-dynamics simulation of the synthesis of intermetallic Ti-Al, Intermetallics 49 (2014) 106–114.
[50] Thomas Edward James Edwards, Fabio Di Gioacchino, William John Clegg, An experimental study of the polycrystalline plasticity of lamellar titanium aluminide, Int. J. Plast. 118 (2019) 291–319.
[51] Pierre Hirel, Atomsk: a tool for manipulating and converting atomic data files, Comput. Phys. Commun. 197 (2015) 212–219.
[52] Michele Parrinello, Aneesur Rahman, Polymorphic transitions in single crystals: A new molecular dynamics method, J. Appl. Phys. 52 (12) (1981) 7182–7190.
[53] Alexander Stukowski, Visualization and analysis of atomistic simulation data with OVITO–the open Visualization Tool, Modell. Simul. Mater. Sci. Eng. 18 (1) (2009) 015012.
[54] Futoshi Shimizu, Shigenobu Ogata, Ju Li, Theory of shear banding in metallic glasses and molecular dynamics calculations, Mater. Trans. (2007).
[55] Alexander Stukowski, Karsten Albe, Dislocation detection algorithm for atomistic simulations, Modell. Simul. Mater. Sci. Eng. 18 (2) (2010) 025016.
[56] Jörg Karch, Rainer Birringer, Herbert Gleiter, Ceramics ductile at low temperature, Nature 330 (6148) (1987) 556–558.
[57] H. Wilhelm, F. Spieckermann, C. Fischer, G. Polt, M. Zehetbauer, Characterization of strain bursts in high density polyethylene by means of a novel nano creep test, Int. J. Plast. 116 (2019) 297–313.
[58] J.N. Wang, T.G. Nieh, The role of ledges in creep of TiAl alloys with fine lamellar structures, Acta Mater. 46 (6) (1998) 1887–1901.
[59] G.B. Viswanathan, S. Kartikeyan, M.J. Mills, V.K. Vasudevan, Creep properties of a fully-lamellar Ti–48Al–2Cr–2Nb alloy, Mater. Sci. Eng. A 319 (2001) 833–837.

[60] W.R. Chen, J. Triantafillou, J. Beddoes, L. Zhao, Effect of fully lamellar morphology on creep of a near γ-TiAl intermetallic, Intermetallics 7 (2) (1999) 171–178.
[61] Brian D Worth, J. Wayne Jones, John E Allison, Creep deformation in near-γTiAl: Part 1. the influence of microstructure on creep deformation in Ti-49Al-1V, Metall. Mater. Trans. A 26 (11) (1995) 2947–2959.
[62] K. Maruyama, R. Yamamoto, H. Nakakuki, N. Fujitsuna, Effects of lamellar spacing, volume fraction and grain size on creep strength of fully lamellar TiAl alloys, Mater. Sci. Eng. A 239 (1997) 419–428.
[63] W.J. Zhang, S.C. Deevi, Analysis of the minimum creep rates of TiAl alloys, Mater. Sci. Eng. A 362 (1–2) (2003) 280–291.
[64] Yue Fan, Yuri N Osetskiy, Sidney Yip, Bilge Yildiz, Mapping strain rate dependence of dislocation-defect interactions by atomistic simulations, Proc. Nat. Acad. Sci. 110 (44) (2013) 17756–17761.